An Ultrafast X-Ray Streak Camera for Time-Resolved High-Energy-Density Applications

Introduction

The x-ray streak camera is an instrument that is frequently called upon to measure the temporal variation of x-ray signals in ultrafast ($\sim 10^{-12}$ s) experiments. The x-ray streak camera finds use in the fields of spectroscopy[1–3] and imaging[4–7] of high-energy-density (HED) physics experiments, where the temporal duration of the HED material to be examined is set by the inertial confinement time; in the case of highly compressed solid-density plasma, this can be as brief as tens of picoseconds. Characterization of the emitted x rays yields information about the ionization state,[8] electron density,[9] and temperature[10] of the material at a high energy density. This necessitates a streak camera with high temporal resolution ($\sim$ a few picoseconds) and spatial resolution since the system evolves rapidly and experimental measurements require detailed, finely resolved measurements of the x-ray radiation.

Using the x-ray streak camera, one can measure the short-duration x-ray signals through a series of conversions to electrons and visible photons, each with an associated gain and additive noise that serves to increase uncertainty in the measured signal. An x-ray pulse incident on the photocathode of the x-ray streak camera yields a number of photoelectrons with an energy spread of a few electron volts.[11] The electron pulse is accelerated in a high gradient field to kilo-electron-volt energies and then imaged with an electro-optical system onto a phosphorescent screen coupled to a low-noise charge-coupled–device (CCD) array for recording. The intrinsic capability of the x-ray streak camera sets fundamental constraints on the fidelity of experimental studies and therefore requires careful consideration. The comparison of streak image data to models requires a fundamental understanding of the camera's sensitivity, so that enough photons can be measured to adequately constrain the measurement.

In the series of measurements detailed in this article, the performance of the streak camera has been assessed through dynamic tests with a pulsed laser source in addition to static imaging and sensitivity tests with a soft x-ray source. The streak camera is used in a variety of spectroscopic applications[12–14] at LLE. The following sections (1) describe the essential features of the streak camera's imaging system and the experimental setup for characterizing the camera; (2) describe the calibration of the time base in the camera; (3) discuss the best focusing of the tube and the spatial- and temporal-resolution elements of the camera; (4) discuss the intrinsic gain of the camera in terms of recorded CCD electrons per photoelectron associated with this camera configuration; (5) discuss the effect of space-charge broadening and the linear dynamic range of the camera relative to the number of photoelectrons per resolution element; and (6) present a brief discussion of the implications of these measurements.

Camera System Layout

Figure 153.20 shows a layout of the streak camera and the testing apparatus setup. The streak camera described here is the third generation of an x-ray streak system built on the PJX streak tube[15] and Rochester Optical Streak System (ROSS) electronics.[16] The ultrafast sweep pulser was built by Kentech Instruments.[17] The camera consists of a removable photocathode plate, a streak tube that opens directly into the vacuum chamber, a phosphorescent window at the output of the tube, and an image recording system to digitize the phosphor image at the output vacuum window. The photocathode plate holder is interchangeable and the photocathode may be changed based on the experimental application. The photoelectrons generated from the photocathode are accelerated through a 3-kV/mm gradient field via a 5-mm gap and are imaged by a quadrupole-doublet electron focusing geometry. The nature of the doublet allows for two magnification modes to be controlled by the polarity of the quadrupole voltages. The standard polarity mode images a 60-mm × 0.4-mm^2 region of the photocathode with 0.4× magnification. Inverting the polarity of the two quadrupoles reverses the magnifications, which images the central 6 × 0.1 mm^2 of the photocathode. The electrons passing through the slot appear to come from a virtual photocathode[18] focusing electrons from a virtual point source behind the physical photocathode with a spot size ultimately limited by the transverse electron energy distribution.
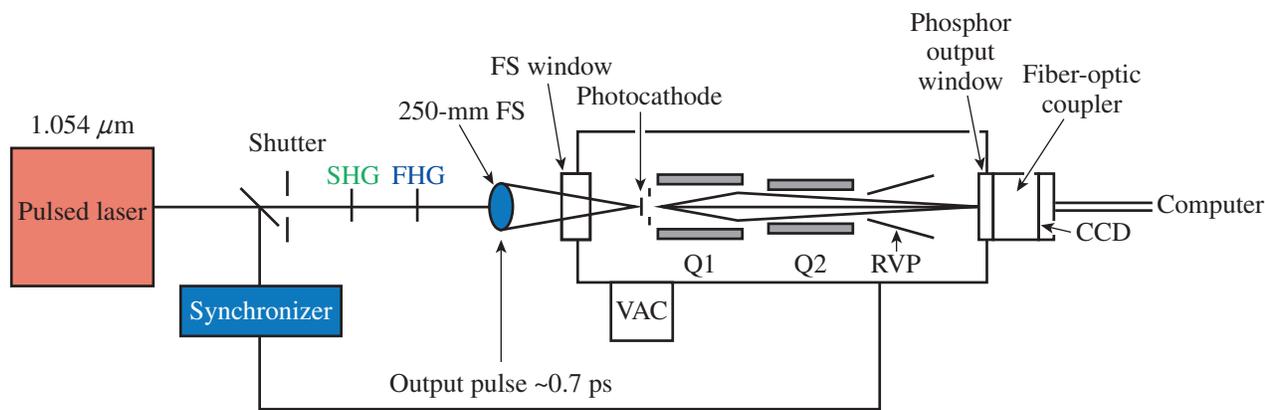
E27038JR

Figure 153.20
The experimental configuration for testing the third-generation x-ray streak camera. A subpicosecond 263-nm laser is pulsed onto the photocathode focused by a 250-mm-focal-length fused-silica double convex lens. The signal is converted to photoelectrons at the photocathode where they are accelerated through a 3-kV/mm gradient field and focused by a quadrupole doublet (QP1 and QP2) and streaked by a high-voltage transient applied to the ramping voltage plates (RVP's) and synchronized to the laser pulse. Photons generated at the phosphor output window are fiber optically coupled to a scientific charge-coupled device (CCD) and readout by computer. FS: fused silica; SHG: second-harmonic generation; FHG: fourth-harmonic generation; VAC: vacuum.

The output screen is recorded by a Spectral Instruments Series 1000 scientific CCD camera with a back-illuminated E2V 42-40 chip with 13.5-μm pixel pitch and free of cosmetic defects. The image from the output screen is relayed to the CCD through an Incom fiber-optic coupler. The CCD is operated at a temperature of –30°C, and the digitization noise from the CCD array is 4.2 photoelectrons; the gain is 0.7 electrons/ADU (analog-to-digital unit) as measured by the photon transfer method of Janesick et al.[19] The streak camera has two sweeping rates, accessed through separate high-voltage pulser circuits, with a window of nominally 1 ns and 5 ns, which were measured in this study.

The final digital output from the camera is a 2048 × 2048 16-bit array. The first dimension of the array corresponds to a spatial view along the length of the slit, where one pixel corresponds to 3 μm in inverse mode and 30 μm in standard mode. The second dimension is an image of the slit that is swept in time across the image.

Experimental Technique
1. Time-Base Calibration
The time base—the relationship between the sweep and on-screen location in the image—was characterized for stability and reproducibility. The streak camera operates by applying fast voltage transients to a pair of deflection plates; a series of such transients were recorded using the camera. The repeatable operation of the stack of the avalanche voltage pulser is necessary to obtain a reliable performance of the sweeping circuit. A subpicosecond (0.7-ps) Nd:glass (1.054-μm) laser pulse[20,21]

is frequency quadrupled to provide a UV pulse suitable for generating photoelectrons on a gold photocathode (200 Å) supported on a 1-μm parylene substrate. Half of the UV pulse is retarded by a quartz plate that provides a calculated fixed delay of 11.2 ps to the pulse with respect to the undelayed beam. The timing between the laser pulse and the streak camera triggering is varied to advance the two pulses across the swept region in the streaked image. This procedure is repeated a number of times across the sweep window. The distance in pixels between the two peaks is recorded along with the location of the two pulses in the streak image. The dwell time per pixel of the signal is calculated by dividing the distance in pixels between the two peaks against the known delay of the quartz plate. A representative image from the camera and the fitted data are shown in Figs. 153.21(a) and 153.21(b), respectively.

The double pulse was time delayed with respect to the ramping voltage trigger to trace out the shape of the deflected beam on the CCD. The results of the sweep rate measurement and a fit are plotted in Fig. 153.22(a). The data show a dwell time that is, at a minimum, close to the center of the sweeping window. A fourth-order polynomial fit is calculated to parameterize the sweep speed as a function of the on-chip location. The uncertainty in the time base originates from the fact that the ramp voltage applied to the deflection plates for each sweep is slightly different on each triggering. In the data set in Fig. 153.22(a), each point on the plot represents an independent sweep and therefore a sample of the distribution of possible sweep rates at that location. An envelope of possible sweep rates [shown by

the $\pm 2\sigma$ curves on either side of the fitted data in Fig. 153.22(a)] gives a bound on the possible sweep rates for an independent sweep. This is converted to the time base uncertainty by calculating the cumulative sum of the bounds to the fits. This is shown in Fig. 153.22(b), with the fitted time base and possible other time bases. Over the entire swept window, this cumulative

sum adds to 40 ps over the 900-ps record length, which yields a systematic uncertainty in the measurement of two points in time of <5%. The results are listed in Table 153.IV. With the time base measured, the impulse response of the camera is also characterized by measuring the apparent temporal width of the subpicosecond pulse.
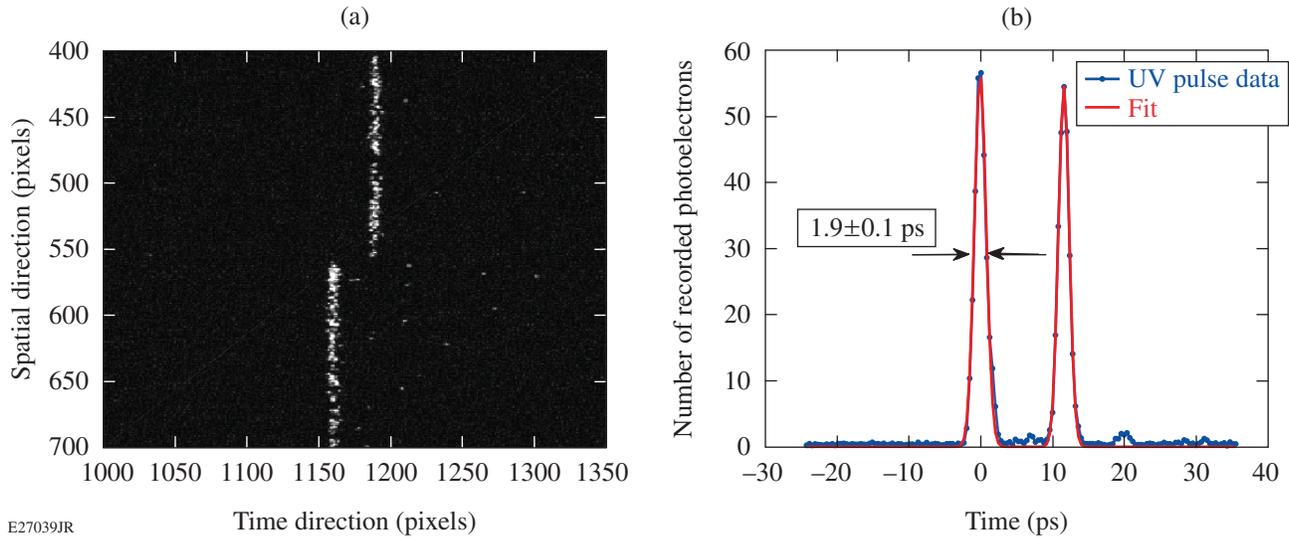
Figure 153.21
(a) Swept image of the split UV pulse on the streak-camera CCD obtained with a subpicosecond pulse split by an etalon of fused silica yielding an 11.2-ps delay between the two pulses; (b) lineout image of (a) and Gaussian fits of the two pulses.
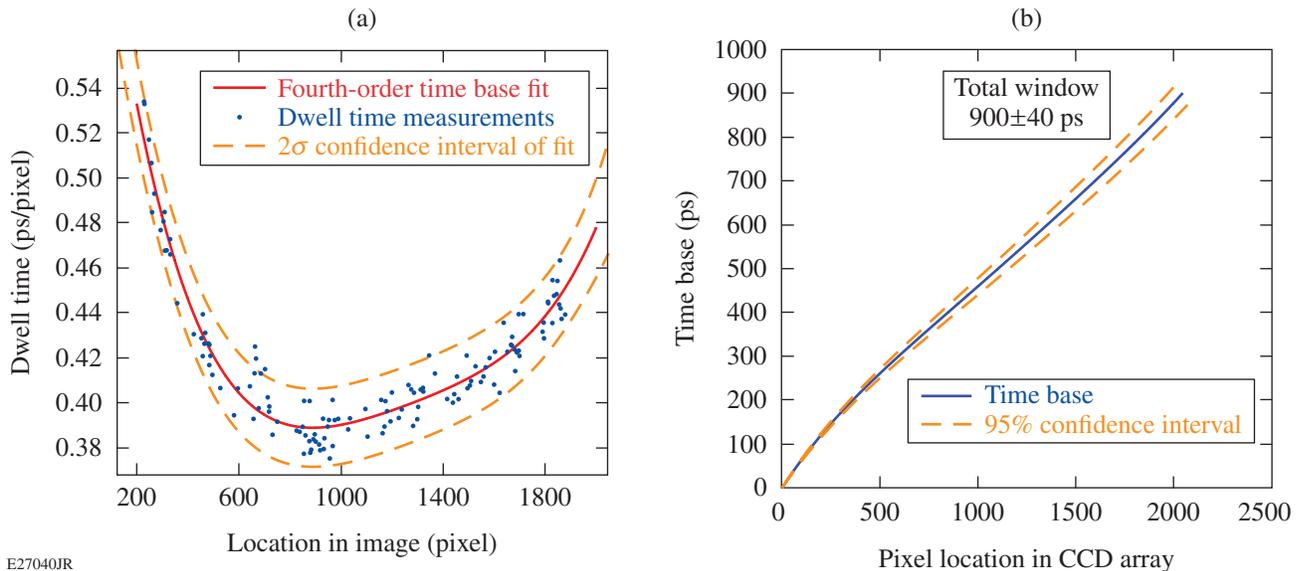
Figure 153.22
(a) The dwell time per pixel as a function of pixel location on the sweep window for the camera using the fast pulser; (b) the camera time base as a function of position on the CCD array.

Table 153.IV: Sweep window measurements.

	Sweep window	Impulse response
Voltage pulser 1	900±40 ps	1.9±0.1 ps
Voltage pulser 2	4.6±0.2 ns	0.01±0.005 ns

Note: Absolute timing is ultimately limited by the jitter in the ramp trigger circuit, which was measured to be <20 ps.

Table 153.IV gives the fitting parameters for the streak-camera sweep rate. The average sweep rates for the two speeds are 0.43 and 2.2 ps/pixel for each sweeping rate, respectively. The fastest portion of the fast sweep has a peak sweep rate of 0.39 ps/pixel. The impulse response of the camera is ~2 ps in this region, measured by fitting the detected subpicosecond pulse. The corresponding full temporal windows were found to be 900 ps and 4.6 ns for the two sweeping speeds.

Focus Optimization

The streak camera's electro-optical imaging system consists of two quadrupole electromagnets that can be adjusted with an internal electronic control. The best focusing of the streak camera was found by varying the voltage on each quadrupole element and measuring the width of the image on the camera for each voltage configuration. The streak camera was equipped with an x-ray–sensitive photocathode of 3000-Å potassium bromide on a 12.5-μm beryllium substrate and illuminated with a large-area, uniform soft x-ray source. The soft x-ray source is a gold bombardment target on a 12.5-μm Be substrate operated in transmission that generates x rays in the 1- to 6-keV range, limited by the transmission of the Be in the low-energy range and the 6-kV electron source at high energy. In the resulting static image, the width of the image of the slit in the swept direction and the contrast of a spatial fiducial bar and space mask in the spatial direction were measured. Figures 153.23(a) and 153.23(b) show contours of each of the fitted parameters as a function of the voltage applied to each electron optic. In the spatial resolution direction, the width is assessed using the following formula:

$$M = \frac{4}{\pi} e^{-2(\pi\sigma\nu)^2},$$

where M is the contrast of a square wave mask with spatial frequency ν and σ is the $1/e$ width of a gaussian line spread function.[22] In the temporal direction, the width is assessed by finding the full width at half maximum (FWHM) of the line focus. The best-focus voltages are determined through a simultaneous minimization of a merit function that considers equally the temporal and spatial impulse responses. The minimum resolution elements in the spatial and temporal axes are reported in Table 153.V.

Table 153.V: Summary of streak-camera calibration measurements.

	Standard mode	Inverse mode
Temporal resolution (fast sweep)	9 ps	2.1 ps
Magnification (designed)	(0.4×)	(4×)
Spatial resolution at photocathode plane	70 μm	18 μm
Number of spatial resolution elements	>800	>300
Number of temporal resolution elements	~100	400
Dynamic range per resolution element (fast sweep)	225:1	30:1
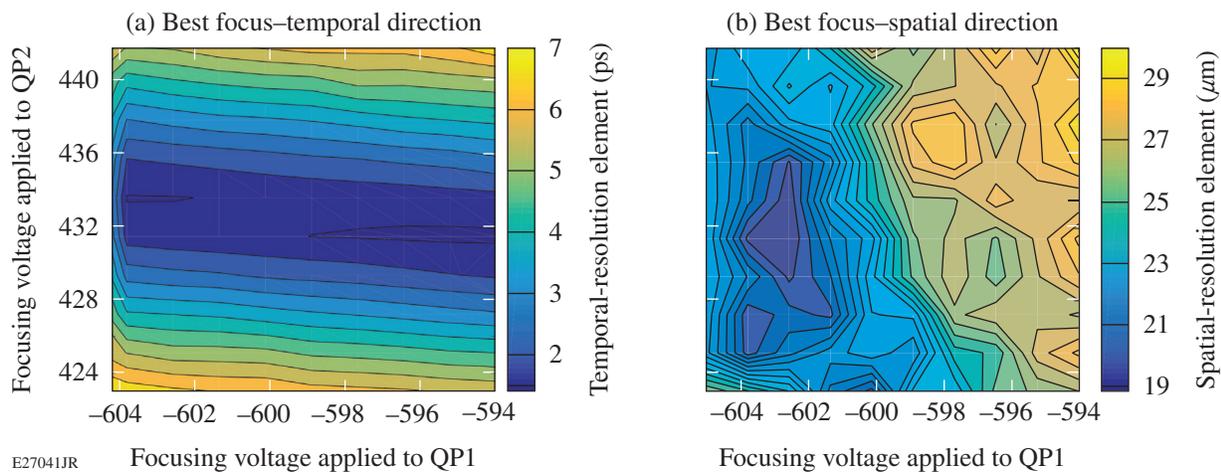
Figure 153.23
(a) The measured width of the detected pulse and (b) spatial resolution element as functions of focusing voltages on each quadrupole.

The focusing voltages with which to best focus the camera are compared against a static particle-tracking code SIMION model of the designed geometry and are found to agree to design predictions by 5%. This discrepancy between the model and experimental results is attributed to the stackup of manufacturing tolerances within the electron optical system.

Gain and Secondary Electron Production

The streak-camera gain and noise figure was also characterized. The streak-camera gain is the enhancement in the number of electrons from the photocathode to the streak camera for a given extraction voltage, phosphor, and image relay system to the detector, typically measured in CCD electrons per accelerated photoelectron. It is essential to accurately measure the system's gain since the photoelectron current is the limiting factor in streak-camera measurements. The noise factor is a multiplicative factor that characterizes the relative increase in variance of the output signal relative to a theoretical noise-free amplification. The raw signal from the streak camera must ultimately be converted to detected photoelectrons, which requires a knowledge of the gain. The statistical variance of the output signal σ_{out}, in CCD electrons, follows from the variance theorem that uncorrelated variances add in quadrature,

$$\frac{\sigma_{out}^2}{S_{out}^2} = \frac{\sigma_G^2}{G^2} + \frac{\sigma_{in}^2}{S_{in}^2},$$

where S_{out} is the output signal in CCD electrons, G is the signal gain, σ_G is the variance arising from the gain process, S_{in} is the input signal in photoelectrons, and σ_{in} is the input variance. The input signal (arrival of photoelectrons) is naturally Poisson distributed (i.e., $\sigma_{in}^2 = S_{in}$) and the mean output signal S_{out} is the input signal times the gain G.

By rearranging, it is apparent that the output variance is increased by a factor F^2 compared to a perfect application of gain (i.e., $\sigma_{out}^2 = S_{out}G$):

$$\sigma_{out}^2 = S_{in}G^2\left(\frac{S_{in}\sigma_G^2}{G^2} + 1\right) = S_{out}GF^2.$$

The method for determining the gain of the streak camera and the secondary electron spectrum of the x-ray photocathode has been laid out in Ref. 23. Here we follow a similar scheme in order to isolate the intrinsic gain of the camera and the number of secondary electrons from the photocathode.

The single photoelectron gain is measured by illuminating a gold-coated parylene-N photocathode with 263-nm laser light. The illumination is kept low so that single-photon–electron events dominate the signal, and the arrival of two photons at the same location at the same time is unlikely. UV illumination on a gold photocathode produces one photoelectron per absorbed photon. The pulse-height distribution of the signal is shown in Fig. 153.24.

E27042JR
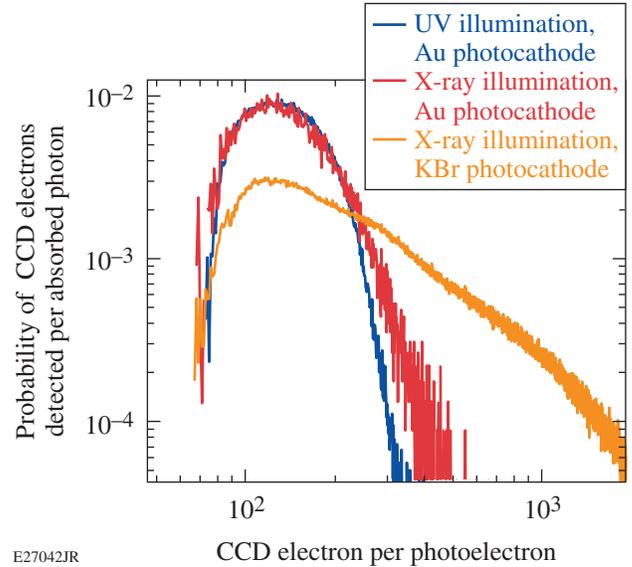
Figure 153.24
Histograms of pulse-height values from illumination with UV and soft x-ray radiation. Generation of multiple electrons per absorbed photon tends to broaden the distribution, leading to a higher gain at the expense of greater noise in the detected signal. The mean values and variance of each of the distributions are given in Table 153.VI.

Table 153.VI: Streak-camera gain.

Material	Gain	σ_G	F^2	Electrons per absorbed photon
263-nm illumination, Au photocathode	131	57	1.19	1.00
X-ray illumination, Au photocathode	167	83	1.25	1.27
X-ray illumination, KBr photocathode	403	380	1.80	2.83

A pulse-height distribution of the sparse photo events is created by binning over a super pixel centered on each event. The super pixel size was determined by collecting and averaging 20,000 single-photon events and characterizing the average size in pixels of the single-photon event. The 1/e width of the aver-

age single-photon event was found to be 0.56 pixels, indicating that 99.8% of CCD counts are located within a 3×3 super pixel of the peak for a single-photon event. The number of ADU's inside the super pixel is counted and recorded in a histogram. The CCD ADU-to-electron conversion was applied to convert the units to electrons.

The pulse-height distribution is constructed in the following manner: The images are corrected for bias and dark current generation with a 200 frame average of dark frames acquired prior to each run. This creates a high signal-to-noise (SNR) dark frame from which to subtract the sparse illuminated image. Individual spurious events arising from the transit of high-energy particles, commonly referred to as cosmic rays in CCD literature, are eliminated from the dark frame through a five-frame median filter of the dark-frame stack. The number of pixels removed as a result of such spurious events is counted; this number is typically 2 to 5 ppm, corresponding to <21 events over the 2048×2048 chip in the image.

In a typical x-ray photocathode interaction with an insulator such as potassium bromide, one x-ray photon can generate a multitude of secondary photoelectrons.[11] An x-ray photon has significantly higher energy than the photoelectric work function of the photocathode, so the primary photoelectron emerges with significant kinetic energy. The mean-free path of an electron inside the photocathode is small compared to the thickness of the layer, and the primary electron undergoes a number of collisions before emerging out the other side of the photocathode. By dividing the number of CCD electrons recorded for KBr by the intrinsic gain measured for UV on gold illumination, we find that the KBr photocathode yields $2.8\times$ the number of photoelectrons to the phosphor per absorbed x ray. It is important to note that this measurement was made *in situ* and includes losses in the electro-optical imaging system and the current condition of the photocathode layer.

Space-Charge Broadening

The effect of space-charge broadening is measured by observing the increase in the apparent width of the photo-electron signal from a fixed pulse width as a function of the extracted number of photoelectrons per picosecond. In this evaluation, the streak-camera ramp circuit is synchronized to the laser pulse and the UV laser spot is focused onto the photo-cathode to provide a locally intense signal. The laser spot was measured to be 100 μm in diameter, which is well suited to the photocathode width in inverse mode (~90 μm). The laser pulse

is filtered to the minimum detectable signal (~1 photoelectron per pulse) and progressively increased in intensity while measuring the pulse width from the streak camera.

The measured signal width is plotted against the number of extracted photoelectrons per resolution element in Fig. 153.25. In the inverse mode, the effects of space-charge broadening become apparent near 30 detected photoelectrons per resolution element in the inverse mode, which signals the upper limit to the dynamic range of the camera. The limit imposed is a 20% broadening of the camera's impulse response in each operating mode—the total dynamic range for this event. The camera is capable of detecting single photoelectron events (~130 CCD electrons per event for UV/Au) above the noise floor (13.2 CCD electrons per resolution element) of the CCD's recording system, providing a lower limit of one photoelectron per resolution element in both operating modes.

E27043JR
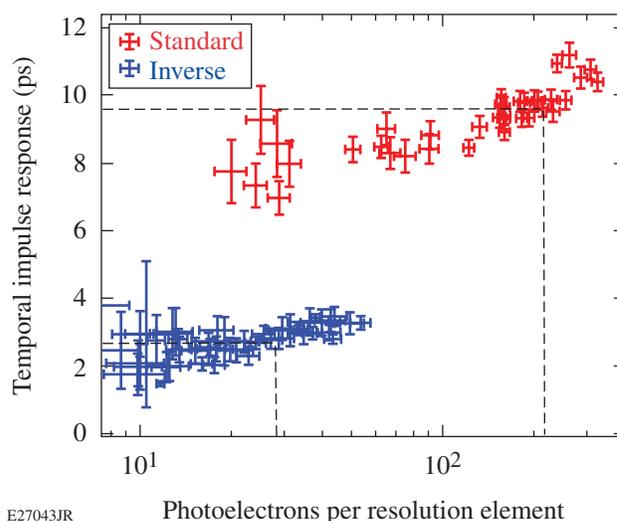
Figure 153.25
Measured FWHM broadening trends for inverse and standard modes as a function of photoelectron number per resolution element. Dashed lines show 20% temporal broadening in the horizontal direction and the recorded signal per resolution element in the vertical direction.

The predominant limiting factor in the streak camera's dynamic range is space-charge broadening. For this camera, the effect is most pronounced at the photocathode, where the electrons have yet to be accelerated and photoelectron current density is the highest. The lower magnification of the standard mode allows a lower current density per resolution element at the photocathode and ultimately a higher dynamic range. When selecting a photocathode material, consideration of

space-charge limits depends on the number of photoelectrons per absorbed photon since the space-charge limit is imposed on the amount of accelerated charge, not the number of absorbed photons. In this case, the dynamic range is reduced by the number of secondary electrons emitted by the photocathode.

Conclusion and Operation Recommendations

The PJX-3 x-ray streak camera has been evaluated for experiments in the future. The time base and associated uncertainty were quantified to 5% with a variable-delay subpicosecond laser pulse that was scanned through the sweep window. The intrinsic gain of the camera was measured and used to determine the average value and spread of CCD ADU's per single photoelectron created at the photocathode. The effect of space-charge broadening was characterized and seen to limit the total dynamic range per resolution element. Accurate measurements of time base and photometric gain and added noise are essential to quantifying measurements and associated uncertainty made with the streak camera. A summary of the performance is listed in Table 153.V.

Following from the analysis in this article, it is advised to disperse the signal as much as possible over the streak-camera slit to maximize the useful dynamic range of the system; locally bright features will cause space-charge broadening and distortions, rendering data difficult to reduce from the streak-camera image. In the case of a very large dynamic range in the source (e.g., x-ray satellite lines near a resonance line), it may be advisable to use different photocathode materials for different parts of the spectra to avoid saturating the main peak while maintaining a sufficient signal in the weaker feature.

REFERENCES

1. S. P. Regan, J. A. Delettrez, R. Epstein, P. A. Jaanimagi, B. Yaakobi, V. A. Smalyuk, F. J. Marshall, D. D. Meyerhofer, W. Seka, D. A. Haynes, Jr., I. E. Golovkin, and C. F. Hooper, Jr., Phys. Plasmas **9**, 1357 (2002).

2. R. Shepherd *et al.*, Rev. Sci. Instrum. **75**, 3765 (2004).

3. E. V. Marley *et al.*, Rev. Sci. Instrum. **83**, 10E106 (2012).

4. Y. P. Opachich *et al.*, Rev. Sci. Instrum. **83**, 125105 (2012).

5. D. G. Hicks, B. K. Spears, D. G. Braun, R. E. Olson, C. M. Sorce, P. M. Celliers, G. W. Collins, and O. L. Landen, Phys. Plasmas **17**, 102703 (2010).

6. D. G. Hicks, B. K. Spears, D. G. Braun, R. E. Olson, C. M. Sorce, P. M. Celliers, G. W. Collins, and O. L. Landen, Rev. Sci. Instrum. **81**, 10E304 (2010).

7. K. Shigemori *et al.*, Rev. Sci Instrum. **83**, 10E529 (2012).

8. O. Ciricosta *et al.*, Phys. Rev. Lett. **109**, 065002 (2012).

9. J. Ashkenazy, R. Kipper, and M. Caner, Phys. Rev. A **43**, 5568 (1991).

10. R. S. Marjoribanks, M. C. Richardson, P. A. Jaanimagi, and R. Epstein, Phys. Rev. A **46**, R1747 (1992).

11. B. L. Henke, J. Liesegang, and S. D. Smith, Phys. Rev. B **19**, 3004 (1979).

12. S. T. Ivancic, C. R. Stillman, D. Nelson, I. A. Begishev, C. Mileham, P. M. Nilson, and D. H. Froula, Rev. Sci. Instrum. **87**, 11E538 (2016).

13. C. R. Stillman, P. M. Nilson, S. T. Ivancic, C. Mileham, I. A. Begishev, R. K. Junquist, D. J. Nelson, and D. H. Froula, Rev. Sci. Instrum. **87**, 11E312 (2016).

14. P. M. Nilson, F. Ehrne, C. Mileham, D. Mastrosimone, R. K. Jungquist, C. Taylor, C. R. Stillman, S. T. Ivancic, R. Boni, J. Hassett, D. J. Lonobile, R. W. Kidder, M. J. Shoup, A. A. Solodov, C. Stoeckl, W. Theobald, D. H. Froula, K. W. Hill, L. Gao, M. Bitter, P. Efthimion, and D. D. Meyerhofer, Rev. Sci. Instrum. **87**, 11D504 (2016).

15. O. V. Gotchev, P. A. Jaanimagi, J. P. Knauer, F. J. Marshall, and D. D. Meyerhofer, Rev. Sci. Instrum. **75**, 4063 (2004).

16. P. A. Jaanimagi, R. Boni, D. Butler, S. Ghosh, W. R. Donaldson, and R. L. Keck, Proc. SPIE **5580**, 408 (2005).

17. Kentech Instruments Ltd., Wallingford, Oxfordshire, OX10 8BA, UK.

18. P. A. Jaanimagi, A. Mens, and J.-C. Rebuffie, Proc. SPIE **2549**, 62 (1995).

19. J. R. Janesick, K. P. Klaasen, and T. Elliott, Opt. Eng. **26**, 261072 (1987).

20. V. Bagnoud, J. Puth, I. Begishev, M. Guardalben, J. D. Zuegel, N. Forget, and C. Le Blanc, in *Conference on Lasers and Electro-Optics/Quantum Electronics and Laser Science and Photonic Applications, Systems and Technologies*, Technical Digest (CD) (Optical Society of America, Washington, DC, 2005), Paper JFA1.

21. V. Bagnoud, J. D. Zuegel, N. Forget, and C. Le Blanc, Opt. Express **15**, 5504 (2007).

22. C. Kunz, R. Haensel, and B. Sonntag, J. Opt. Soc. A **58**, 1415 (1968).

23. S. Ghosh, R. Boni, and P. A. Jaanimagi, Rev. Sci. Instrum. **75**, 3956 (2004).